Numerical Study on the Shear Failure and Load Transfer Mechanism of Helical Piles in Cohesionless Soils under Axial Compressive Loading

Ignatius Tommy Pratama*, Anastasia Sri Lestari, Ivan Oktavianus

Civil Engineering Department, Faculty of Engineering, Parahyangan Catholic University, Ciumbuleuit Street, No. 94, 40141, INDONESIA
*Corresponding author: tommyignatius@unpar.ac.id

ABSTRACT The methods employed to calculate the axial bearing capacity of a helical pile depend on the shear failure model around the pile, which is also influenced by the spacing and diameter of the helical plates. However, studies on the transition of the failure mode and the load transfer mechanism with the change of helical plate spacing and diameter in cohesionless soil subjected to axial compressive load were limited. Thus, this paper investigated the effects of helix diameter and spacing on the axial compressive load-bearing capacity, shear failure model, and load transfer mechanism of helical piles with two helical plates embedded in the homogeneous medium and dense sands, as well as in the stratified medium to very dense sand. Axial loading tests on helical piles with various helix diameters and spacings were simulated using a two-dimensional finite element program with axisymmetric modeling to obtain the load-settlement curve, which was later used to estimate the ultimate bearing capacity of the helical piles. The ultimate bearing capacity of the helical piles was also computed using the conventional methods, i.e., the individual bearing and cylindrical shear methods, and then compared to the numerical-based axial bearing capacity. The stress-strain behaviors of pile and soil were modeled using the Linear Elastic and Mohr-Coulomb material models, respectively. The results show that the numerical-based ultimate bearing capacity of a helical pile increased with increasing the diameter and spacing of the helix. However, the ultimate bearing capacity computed using conventional methods did not show this trend. Then, the transition from the cylindrical shear to the individual bearing failure mechanism occurred at a spacing ratio (i.e., helical plate spacing divided by its diameter) of about two. Ultimately, the load transfer curves indicate that the helical plates mainly supported the applied load.

KEYWORDS Helical Pile; Pile Bearing Capacity; Failure Mechanism; Load Transfer.

1 INTRODUCTION

A helical pile, also known as a screw pile, is a type of drilled pile foundation consisting of helical-shaped circular steel plates, or helical plates, welded at specific intervals along the steel pile shaft. It can be used in various soil conditions and soft rock with an ultimate bearing capacity of less than 7 MPa to support lateral, pullout, and compressive loads (Livneh and El Naggar, 2008; Perko, 2009). In contrast to the conventional pile foundation, the load-carrying mechanism of the helical piles depends not only on the shaft and tip resistances but also on the resistance of the helical plates (Mitsch and Clemence, 1985; Rao et al., 1991).

Studies on the bearing capacity of helical piles indicated two approaches to computing their ultimate axial bearing capacity, known as the cylindrical shear (CS) method and the individual bearing (IB) method. Those methods correspond to different shear failure models. The IB model was initially introduced by Trofimenkov and Mariupolskii (1965) for helical piles with a single helical plate. Later, Adams and Klym (1972) extended the method to helical piles with multiple helical plates. In this approach, shear failure is assumed to occur at each helical plate, meaning that each helical plate contributes to determining the ultimate bearing capacity

of the helical pile in addition to the shaft and tip resistances. As the number of helical plates increases, the ultimate bearing capacity also increases. This IB model is applicable to helical piles with one or more helical plates.

The CS model for helical piles embedded in sands was initially introduced by Mitsch and Clemence (1985), while, Mooney et al. (1985) later, extended this model to helical piles embedded in clay and silt soils. The CS failure model assumes that shear failure occurs between the lowermost and uppermost helical plates, forming a cylindrical shape (Vignesh and Mayakrishnan, 2020). Consequently, the total axial capacity of the pile comprises the shaft, tip, and shear resistance along the failure surface (Sakr, 2009, 2011; Vignesh and Mayakrishnan, 2020). Unlike the IB model, the CS model is suitable for helical piles with two or more helical plates (Mohajerani et al., 2016). Figure 1 illustrates the components of a helical pile that govern the ultimate bearing capacity in the CS and IB methods. Although the IB and CS models are fundamentally different, it is worth noting that shear failure will still adhere to the IB model if the spacing between helical plates is large enough (Adams and Klym, 1972).
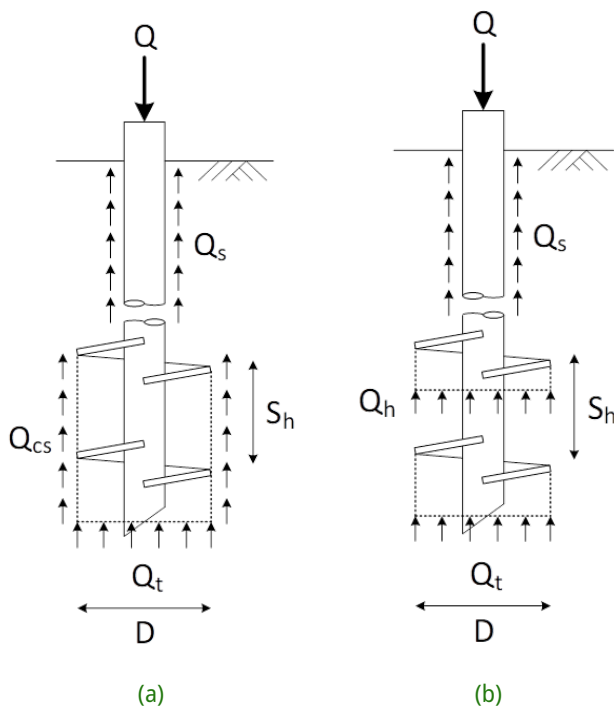
Figure 1 (a) Cylindrical shear and (b) individual bearing capacity methods. Q is the applied load, S_h is the spacing between helical plates, D is the helical plate diameter, Q_s is the shaft resistance, Q_h is the individual helical plate resistance, Q_{cs} is the resistance developed along the CS failure surface, and Q_t is the bottom-end helical and shaft tip resistance.

Sakr (2009) and Vignesh and Mayakrishnan (2020) noted that a larger spacing between helices can shift the failure mechanism from the CS model to the IB model in helical piles. Previous studies showed that the IB shear failure model occurred at a spacing ratio (the ratio of helical plate spacing (S_h) to the helices diameter (D)) ranging from 1.5 to 3, depending on the soil type (Rao et al., 1991; Lutenegger, 2009; Sakr, 2009; Salhi et al., 2013; Nabizadeh and Choobbasti, 2017). However, determining the precise transition point of the shear failure model has been challenging, especially for helical piles embedded in cohesionless soils. Perko (2009) suggested that an ideal spacing of helical plates is achieved when the bearing capacity computed using the IB and CS methods is equal. Furthermore, the proposed S_h/D ratio indicating the transition of the shear failure is primarily estimated based on displacement contours around the helical plates (Alwalan and El Naggar, 2021; Salhi et al., 2013). Therefore, further investigation into shear failure in helical piles is necessary to confirm the developed shear bands along the helical plates, not only by studying deformation contours but also by examining deviatoric shear strain contours. In addition, as pointed out by Mohajerani et al. (2016), further research is needed to understand how the failure mechanism changes due to helical plate spacing, as different studies have reported varying required spacings to induce a change in the failure mechanism.

Furthermore, numerous studies have investigated the

load transfer mechanism of helical piles in cohesionless soil under axial load, utilizing various numerical approaches and laboratory model tests (Livneh and El Naggar, 2008; Soltani-Jigheh and Zahedi, 2020; Alwalan and El Naggar, 2021). However, most of these studies have primarily focused on analyzing displacement contours and load-settlement responses of the pile to elucidate the load transfer behavior, particularly concerning changes in the failure model due to variations in helical plate spacing. Consequently, there has been limited exploration into the mechanism of load propagation from the pile head to the helical plates and the pile toe in previous research effort.

Thus, this paper aims to study the change in the ultimate bearing capacity of helical piles embedded in sandy soils, as well as their shear failure and load transfer mechanisms when subjected to axial compressive load, due to the variations in helical plate diameter and spacing. This research was conducted as follows: Firstly, conventional methods for computing the ultimate bearing capacity of a helical pile in sand soil were first reviewed. Then, a series of axial loading tests on helical piles embedded in homogeneous medium and dense sands, featuring various helical plate diameters and spacing, were simulated using a two-dimensional finite element program, namely PLAXIS 2D. The resulting load-settlement curves, displacement, and deviatoric shear strain contours around the helical piles were then analyzed to describe the effects of helical plate diameter and spacing on the helical pile's ultimate bearing capacity, later denoted as the numerical-based ultimate bearing capacity and its failure mechanism. Moreover, the numerical-based ultimate bearing capacities were compared to those estimated using the conventional methods to evaluate the suitability of the assumed failure mechanism in the conventional methods against the obtained shear failure model in numerical simulation. Subsequently, the load transfer mechanism in helical piles was discussed based on the presented load transfer curves in this paper. The results were eventually verified using a loading test case history of a helical pile installed in cohesionless soil. This study provides insight into load transfer and failure mechanisms in helical piles embedded in cohesionless soil. Additionally, this paper aims to serve as a reference for engineers in selecting the appropriate method for estimating the bearing capacity of a helical pile.

2 METHODS

2.1 Conventional Method for Computing Helical Pile Axial Bearing Capacity

2.1.1 Cylindrical Shear Method

Mitsch and Clemence (1985) proposed an equation to compute the ultimate compressive bearing capacity

(Q_u) of a helical pile embedded in cohesionless soil as follows:

$$Q_u = Q_{cs} + Q_t + Q_s \qquad (1)$$

where each component is illustrated in Figure 1 and can be computed using the following equations:

$$Q_{cs} = \frac{1}{2}\pi D_a \gamma'(H_b^2 - H_t^2)K_s tan\phi' \qquad (2)$$

$$Q_t = \gamma' H A_H N_q \qquad (3)$$

$$Q_s = \frac{1}{2}P_s H_{eff}^2 \gamma' K_s tan\phi' \qquad (4)$$

$$N_q = 1 + 0.56(12\phi')^{\phi'/54} \qquad (5)$$

where D_a is the average helix diameter, γ' is the effective soil unit weight, H_b is the depth of the bottom helix, H_t is the depth of the top helix, K_s is the coefficient of lateral earth pressure in compression loading, ϕ' is the effective soil friction angle, H is the embedment depth of the pile, A_H is the area of the bottom helix, N_q is the dimensionless bearing capacity factor proposed in Supportworks Technical Manual (Deardoff et al., 2021), P_s is the perimeter of the helical pile shaft, and H_{eff} is effective shaft length, which is equal to the depth to the top helix minus the diameter of the top helix (D). According to Fitriana and Hamdhan (2018), the K_s value can be estimated using the following equation:

$$K_s = \frac{\beta}{tan\delta} \qquad (6)$$

where β is the skin friction coefficient based on the soil type and pile construction method (Canadian Geotechnical Society, 2006), and δ is the friction angle between soil and pile. In this study, the δ value was equal to 0.6 ϕ' (Kulhawy, 1986), whereas β was assumed to be 0.8 for medium sand and 1 for dense sand. It is important to note that Equations (2) to (5) are applicable for helical piles with an embedment ratio $H/D \geqslant 5$, where H is the embedment length. For $H/D < 5$, the shaft friction can be neglected (Nasr, 2004).

2.1.2 Individual Bearing Method

Perko (2009) defines the Q_u value based on the IB method as the sum of each helical bearing plate's bearing capacity plus the friction along the shaft. Equation (7) expresses the equation to compute the IB-based Q_u value as follows:

$$Q_u = \Sigma Q_{h,i} + Q_t + Q_s \qquad (7)$$

where $Q_{h,i}$ is the ultimate bearing capacity of the ith helical bearing plate, and i is the number of helical bearing plates. Q_h can be calculated using Equation (3) with A_H as the bearing plate's net area, which is equal to $0.25\pi(D^2 - d^2)$, where d is the shaft diameter. Similarly, Equations (3) and (4) can be used to compute the Q_t and Q_s values of the IB method, respectively. Note that the units used in Equations (1) to (7) must be consistent and follow the unit system used in the calculation. For example, if the depth is denoted in meters, the γ' is in kN m^{-3}, and ϕ' is in degrees, then the unit of Q_u is kN.

2.2 Case Study

The case study used in this paper was based on an axial compressive load test on a double-helix pile, as described by Sakr (2009). The helical pile had a 324 mm round shaft diameter (d) and a 762 mm helix diameter (D) with a shaft and helical plate thickness of 9.5 mm and 25.4 mm, respectively. The helical plates were spaced at three times their diameter (3×D). The pile was embedded in stratified sand soil layers to a depth of 9 m. Generally, the soil stratigraphy consisted of a medium to very dense sand layer extending from the ground surface to a depth of 11.4 m and a dense to very dense soil layer located at 11.4 m to 33 m. The groundwater level (GWL) was located 3.6 m below the ground surface.

2.3 Numerical Simulation and Back Analysis

This study utilized a two-dimensional finite element-based program with axisymmetric modeling to simulate the axial compressive load test on helical piles. Initially, the horizontal and vertical boundaries were set to 2 times the pile length (18 m) and 3.5 times the pile length (31.5 m) (Salhi et al., 2013), respectively, to minimize the boundary effects on the load vs. settlement curves. It was worth noting that due to limitations in axisymmetric modeling, the helical plates in this study were simplified to circular disks without pitch (i.e., the vertical distance between two edges of a helical plate.

In the numerical simulation, the stress-strain behavior of the helical pile structure was modeled using soil elements with a linear elastic material model and non-porous drainage type (Bentley, 2023; Salhi et al., 2013). Given that the material used for the helical pile was steel, the unit weight and Poisson's ratio values were assumed to be 78 kN m^{-3} and 0.3, respectively (Salhi et al., 2013). The Young's modulus of the helical pile material was set to 2.1 × 10^8 kN m^{-2} (Look, 2007). To model the interaction between the pile and soil, interface elements were also introduced on the outer surface of the helical pile with an interface parameter (R_{inter}) of
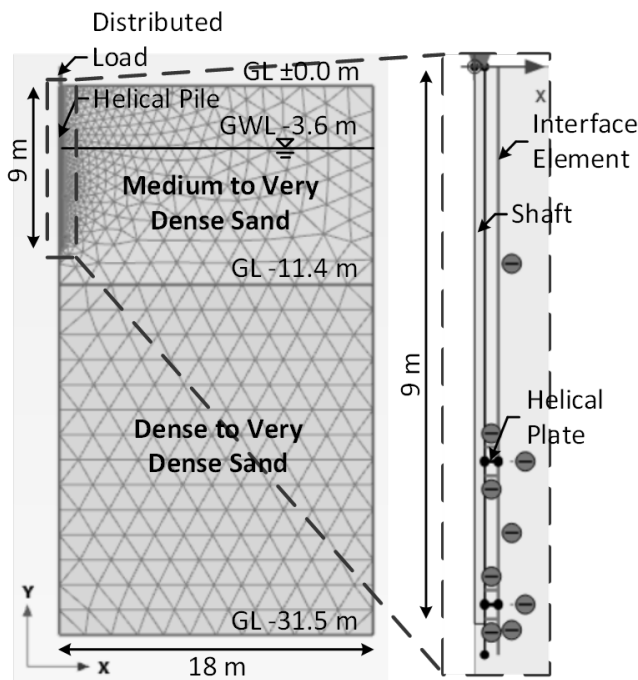
Figure 2 Helical pile model in the finite element program

0.67 (Bentley, 2023). Figure 2 illustrates the helical pile model, the boundaries, the soil stratification, and the mesh distribution in the finite element program.

Back analysis was then performed by matching the load vs. settlement curve obtained from the axial compressive load test in the field with that obtained from the numerical simulation to estimate the parameters of the sand soil layers and to match the soil response to loadings. The simulation stages of the loading test mainly consisted of the K_0-procedure, helical pile installation, and step loading. The K_0-procedure involved generating initial stresses in the soil clusters. The helical pile was then installed. It is important to note that the helical piles in this study were wish-in-place piles; thus, the installation torque was not considered in the simulation. After installation, the axial compressive load was gradually applied to the top of the pile with an increment of 5% of the design load. The settlement of the pile for every load increment was eventually recorded to obtain the load-settlement curve.

In the numerical analysis, the Mohr-Coulomb material model (MC-Model) was adopted to represent the stress-strain behavior of the sands due to the limited soil test data. Although the MC-Model is recognized as a first approximation of soil behavior (Bentley, 2023), it was sufficient to closely predict the soil-pile responses to axial loadings (Elsherbiny and El Naggar, 2013; Livneh and El Naggar, 2008). The drained condition was utilized for the sand layers to prevent excess pore water pressure development. Table 1 lists the estimated soil parameters, including the unit weight of wet soil (γ_n), saturated unit weight (γ_{sat}), effective friction angle (ϕ'), dilatancy angle (ψ'), and the effective Young's

Table 1. Back-Analyzed Soil Parameters

Depth (m)	γ_n (kN/m³)	γ_{sat} (kN/m³)	ϕ' (°)	ψ' (°)	E' (kN/m²)
0.0-11.4	18	20	36	6	115,000
11.4-33.0	20	21	45	15	175,000

Table 2. Parameter Variations for Parametric Study

Variations	Values
Spacing ratio (S_h/D)	0.5, 1, 1.5, 2, 2.5, 3, 3.5
Diameter ratio (D'/D)	0.75, 1, 1.25, 1.5

modulus (E'). The effective Poisson's ratio (υ') for all sand soil layers was assumed to be 0.33. Additionally, the ψ' value could be estimated as ϕ' - 30° according to the PLAXIS 2D material model reference manual (Bentley, 2023).

2.4 Parametric Study

A series of parametric studies were also conducted to investigate the effects of helical plate diameter and spacing on the bearing capacity and failure mechanism of a helical pile embedded in cohesionless soil, utilizing both IB and CS methods. The study involved varying the size and spacing of the helical plate. In this section, double-helix piles with a 9 m embedment length were employed. The parameters and simulated stress-strain behavior of the helical piles were consistent with those used in the back analysis. Table 2 shows the variations of helical plate spacing and diameter, expressed as the spacing ratio (S_h/D) and diameter ratio (D'/D), respectively, where D' represented the modified helix diameter with the D value set at 762 mm. The variations in S_h/D and D'/D ratios were determined based on typical values used in previous studies (Perko, 2009; Rao et al., 1991; Salhi et al., 2013). Additionally, the horizontal and vertical boundaries of the model in the finite element program were maintained at 2 times and 3.5 times the pile length, respectively.

To investigate the effects of helical plate spacing, parametric studies were conducted by varying the S_h/D ratio for helical piles installed in homogeneous medium and dense sands, as well as in stratified soil layers with the parameters described in Table 1. Meanwhile, Table 3 presents the soil parameters for the medium and dense sands, estimated based on typical soil properties for clean sand of appropriate density from Look (2007). Additionally, the effects of helical plate diameter were studied by varying the diameter ratio (D'/D). This analysis was specifically performed for helical piles embedded in stratified soil conditions. For each D'/D ratio, the S_h/D ratio was varied to 0.5, 1.5, 2.5, and 3.5. It is important to note that in these parametric studies, the stress-strain behaviors of the soils and piles remained consis-

Table 3. Homogeneous Soil Parameters

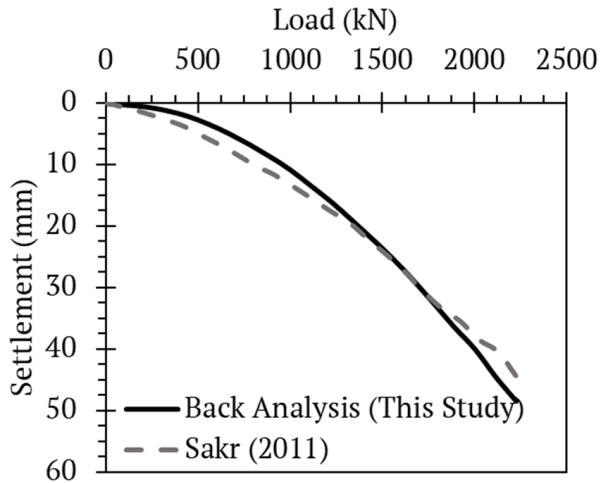| Sand Density	γ_n (kN/m³)	γ_{sat} (kN/m³)	ϕ' (°)	ψ' (°)	E' (kN/m²)
Medium	18	20	36	6	115,000
Dense	20	21	45	15	175,000

Figure 3 Load vs. settlement curve comparison

tent with those used in the back analysis. Furthermore, the groundwater level in all studies was maintained at a depth of 3.6 m below ground level, as shown in Figure 2, to ensure consistency in the analysis results.

The axial compressive load tests were conducted following the same procedure as in the back analysis. The ultimate bearing capacity of a helical pile (Q_u) was then estimated using both the CS and IB methods, applying the formulas outlined in Equations (1) to (7). Additionally, the Q_u, value was also interpreted from the load vs. settlement curve obtained from the numerical simulation. In this study, the Q_u value was defined in accordance with the Federal Highway Administration (FHWA) method (Reese and O'Neil, 1988), where drilled shafts with a 5%D failure criterion were deemed adequate for sandy soils (Elsherbiny and El Naggar, 2013).

3 RESULTS AND DISCUSSION

3.1 Back Analysis

Figure 3 presents the comparison between the load vs. settlement curve obtained from the field (Sakr, 2011) and the numerical simulation. The result depicted in Figure 3 indicates that the soil response to axial loading, considering the soil parameters in Table 1, closely resembled the field condition.

3.2 Effects of Helical Pile Spacing

Figure 4 illustrates the comparison of the Q_u values in homogeneous medium and dense sands, as well as in the stratified soil conditions. In the figure, the Q_u values estimated using the numerical approach are denoted as $Q_{u,FE}$, and represented by circles and straight lines. Meanwhile, the Q_u values computed using the IB ($Q_{u,IB}$) and CS ($Q_{u,CS}$) methods are depicted by diamond and square symbols with straight lines, respectively. Additionally, the red dashed line depicts the relationship between the S_h/D ratio and the modified $Q_{u,IB}$, where the shaft friction between the helical plates was considered in the bearing capacity calculation. Note that the CS and IB methods were used to compute the Q_u values for all S_h/D variations in Figure 4, regardless of the occurred soil shear failure model around the piles. In fact, it is essential to match the calculation method to the actual failure model observed in the field.

The results depicted in Figure 4 illustrate how the spacing between helical plates impacts the Q_u value of the helical pile, with differing effects observed for each soil density. Specifically, denser soil, indicated by higher soil shear strength, resulted in a higher Q_u value. The reason was that dense soil promoted more interparticle contact areas and higher soil frictional resistance, resulting in a higher load that the pile could support. In medium sand, the $Q_{u,CS}$, $Q_{u,IB}$, and the modified $Q_{u,IB}$ values for helical piles exceeded the $Q_{u,FE}$ values. On the contrary, the $Q_{u,FE}$ values closely aligned with the $Q_{u,CS}$ values, particularly in the case of dense sand and stratified soil conditions. This discrepancy may arise from differing interpretations of the Q_u values. It is worth noting that $Q_{u,CS}$ and $Q_{u,BS}$'s represent the bearing capacity of a helical pile under conditions where soil shear strength around the pile is fully mobilized, and the pile is rigid. However, such conditions may not always be realistic. Fully mobilizing the soil shear strength typically requires significant settlement, especially in dense sand, which could damage upper structures. Conversely, the failure criterion of 5%D settlement used to define the finite element-based pile ultimate capacity is a practical settlement level that accounts for pile flexibility and serviceability rather than necessarily representing the settlement at failure (Elsherbiny and El Naggar, 2013).

Then, the $Q_{u,FE}$, and $Q_{u,CS}$ values in Figure 4 increased with increasing S_h/D ratio, but, this trend did not apply to the $Q_{u,IB}$ values. The $Q_{u,IB}$ values decreased as the spacing between helices increased. Initially, it was assumed that this was due to not considering the shaft friction between the helical plates. However, as shown by the red dashed line in Figure 4, the trend of the modified $Q_{u,IB}$ still tended to decrease with increasing S_h/D ratio. Thus, the reason was that, as the upper helical plate moved closer to the ground surface because of
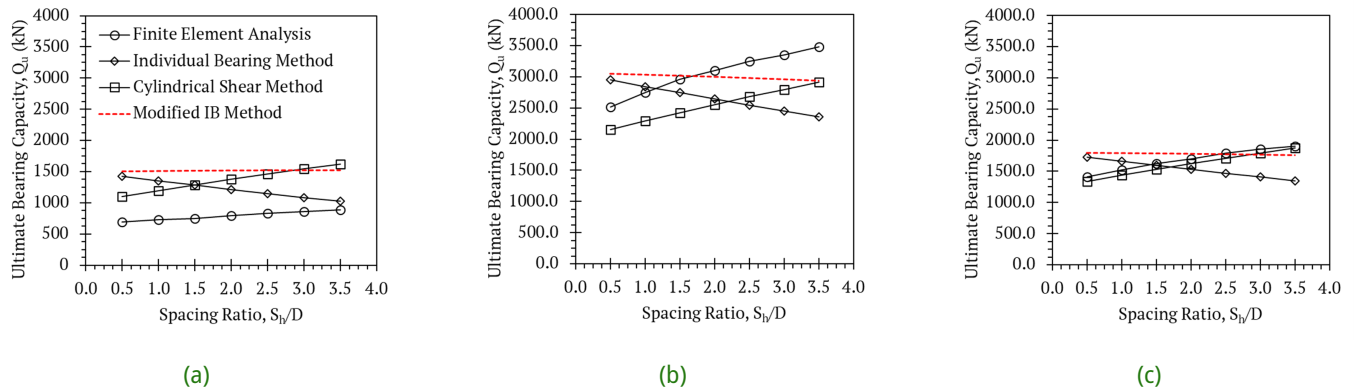
(a) (b) (c)

Figure 4 Ultimate bearing capacity (Q_u) comparison concerning the variations of S_h/D ratio of helical piles in (a) homogeneous medium sand, (b) homogeneous dense sand, and (c) stratified cohesionless soil

increasing in the helical plate spacing, the upper helical plate ($Q_{h,top}$) and upper shaft bearing capacities (Q_s) reduced, while the Q_t remained constant. This phenomenon resulted in a lower $Q_{u,IB}$ for a larger S_h/D ratio. Meanwhile, for the increasing trend of $Q_{u,CS}$, increasing the S_h/D ratio theoretically produced higher Q_{cs} and lower Q_s values. The decrease in Q_s values was smaller than the increase in Q_{cs}, causing an increase in $Q_{u,CS}$ values. In this study, the Q_{cs} increment with increasing S_h/D ratio was almost three times the Q_s decrement. Eventually, the relationship between $Q_{u,FE}$ and S_h/D ratio was relatively similar to the trend of the $Q_{u,CS}$ vs. S_h/D, where larger S_h/D promoted higher $Q_{u,FE}$. Similar findings were also found in Salhi et al. (2013) and Fitriana and Hamdhan (2018). However, this result did not imply that the failure mechanism observed in the numerical simulation was the same as the assumed failure mode by the conventional method. The helical pile failure mechanism based on the numerical approach will be further discussed in subsequent paragraphs. Furthermore, as shown in Figure 4, that considering the shaft friction between the helical plates in the $Q_{u,IB}$ calculation shifted the optimum helical plate spacing ratio, marked by $Q_{u,IB} = Q_{u,CS}$ (i.e., the intersection between $Q_{u,CS}$ vs. S_h/D and $Q_{u,IB}$ vs. S_h/D curves). Perko (2009) suggested that if the S_h/D ratio exceeded the optimum one, it would lead to an excessively long shaft; otherwise, it caused the helical bearing plates to be wasted. In this study, the intersection occurred at $S_h/D = 1.5$ and 2.2 for the homogeneous medium and dense sand cases, respectively, whereas for the stratified soil condition, it was at $S_h/D = 1.7$. Meanwhile, when the modified $Q_{u,IB}$ was adopted, the intersection moved to $S_h/D = 2.9$ for the homogeneous medium sand case, and $S_h/D = 3.5$ for the dense sand case. For the stratified soil conditions, the optimum spacing became $S_h/D = 2.9$. This finding emphasizes that the optimum spacing for helical plates was unique to different site conditions. Additionally, the shaft friction between the helical plates also affected the justification of the theoretical optimum spacing for helical plates. The importance of considering shaft friction between the helical plates will be discussed later. However, such an ap-

proach could not be used for determining the optimum helical plate spacing based on the $Q_{u,FE}$ values. There was no clear distinction between the Q_u values for the CS and IB shear models. The shear failure developed in response to the axial load application in the numerical analysis and it could be determined based on the shear strain and/or deformation contours.

It is important to note that the spacing of helical plates also affects the shear failure development in soil. If the spacing between helices is small enough (i.e., S_h/D is less than 1.5 to 3), the CS failure model is likely to occur, while the IB failure model would occur for S_h/D greater than 1.5 to 3 (Lutenegger, 2011; Salhi et al., 2013). Based on Perko (2009) findings, it is also interesting that, in addition to estimating the optimum spacing, the intersection between $Q_{u,CS}$ vs. S_h/D and $Q_{u,IB}$ vs. S_h/D curves could be used to indicate the change of helical pile shear failure mode from the CS to the IB models. Perko (2009) compared the measured capacity to the predicted capacity, which was determined by the smallest value between $Q_{u,IB}$ and $Q_{u,CS}$, known as the limit state analysis, and found that the measured and the predicted capacities were in good agreement. This finding could indicate that the conventional IB and CS methods could predict the actual Q_u, and the assumed shear failure model in the conventional methods was close to the actual failure in the field. However, as shown in Figure 4, the $Q_{u,FE}$ values were not close to the theoretical minimum Q_u values. The $Q_{u,FE}$ values were generally smaller than the minimum Q_u values for the medium sand case, whereas, for the dense sand case and the stratified soil condition, the $Q_{u,FE}$'s were larger than the minimum Q_u values. Moreover, even though the $Q_{u,FE}$ values were close to the $Q_{u,CS}$ values, especially for the dense sand case and the stratified soil condition, the closeness of the $Q_{u,FE}$ values to the $Q_{u,CS}$ values did not imply that the occurred failure model in the numerical simulation tended always to follow the CS failure mechanism. Therefore, using conventional methods to predict the failure mechanism was not sufficient. The actual failure mechanism should be investigated using either a numerical approach or laboratory
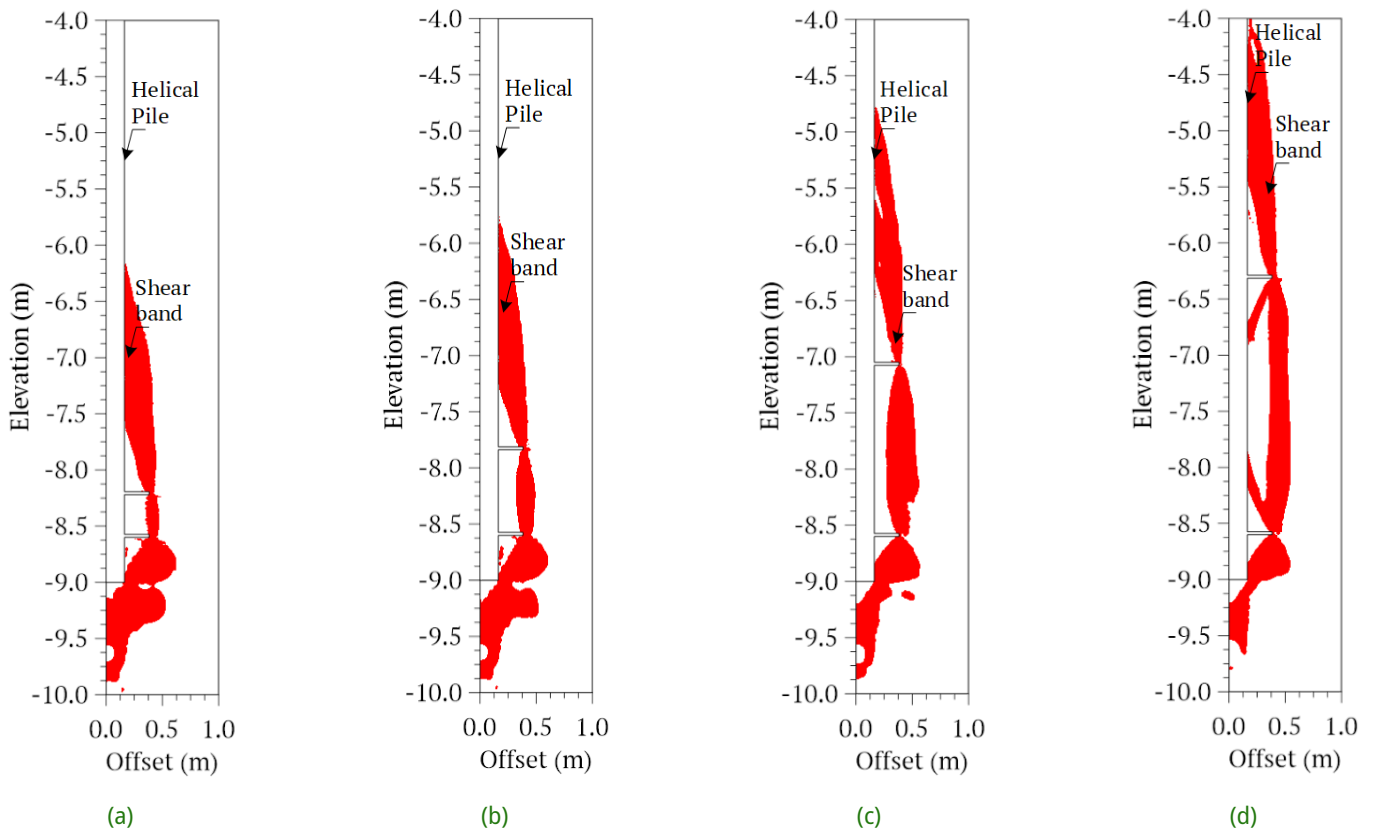
Figure 5 Shear bands around the helical piles embedded in medium sand with $D = 762$ mm and $S_h/D =$ (a) 0.5, (b) 1, (c) 2, and (d) 3 at the pile head load equals 1114 kN

tests by observing the change of shear strain and/or deformation contours to the change of the S_h/D ratio.

The total deviatoric strain (γ_s) contours around the helices were then investigated to further study the developed shear failure around a helical pile under compressive load. The γ_s contours could indicate the development of a shear band along a helical pile. Figures 5, 6, and 7 display the shear band around the helical plates with S_h/D ratios of 0.5, 1, 2, and 3 in medium sand, dense sand, and stratified soil conditions, respectively. The shear bands for the S_h/D ratios of 1.5, 2.5, and 3.5 cases are not shown in this paper due to the space limitation. Each figure also depicts the shear band at a particular load at the pile head. The offset in Figures 5 to 7 denotes the distance from the pile axis.

This study found that the transition of the shear failure occurred at $S_h/D = 2$. As shown in Figures 5 to 7, parts a and b, for $S_h/D \leqslant 2$ cases, the shear band formed from the pile tip to the outer edge of the lower helix (second helix) of the helical pile, then propagated to the outer edge of the upper helix (first helix), and eventually extended to the pile shaft. It was evident that the propagated shear band from the upper to the lower helices formed a cylindrical shape. This form of the shear band was considered a type of CS failure. Furthermore, as the S_h/D ratio increased to $S_h/D > 2$, the IB shear failure model became more apparent. The shear band for

the IB model typically developed at each helical plate, forming from the outer side of the helical plates to the pile shaft, creating a triangle-like form (i.e., in a two-dimensional perspective) as shown in Figures 5 to 7, parts c and d.

The results presented in Figures 5 to 7 were relatively consistent for the helical piles with the same diameter of the helices embedded in all soil densities. However, the shear bands depicted in Figures 5 to 7 were notably different from the assumed shear band in the conventional methods illustrated in Figure 1. The shear bands below the lower helix and above the upper helix in Figure 1 were presumably over simplified in the conventional methods. Furthermore, the S_h/D ratio at which the transition of the shear failure model occurred in this study (i.e., $S_h/D = 2$) was still within the range reported by Lutenegger (2011) and Salhi et al. (2013). Lutenegger (2011) conducted a series of loading tests on helical piles embedded in sand soils and found that the failure mode of helical piles in sand changed from the CS model to the IB model at $S_h/D = 3$. Meanwhile, Salhi et al. (2013) used a numerical approach and found that the transition from the CS model to the IB model for helical piles embedded in sand soil occurred at S_h/D about 1.5 to 2.
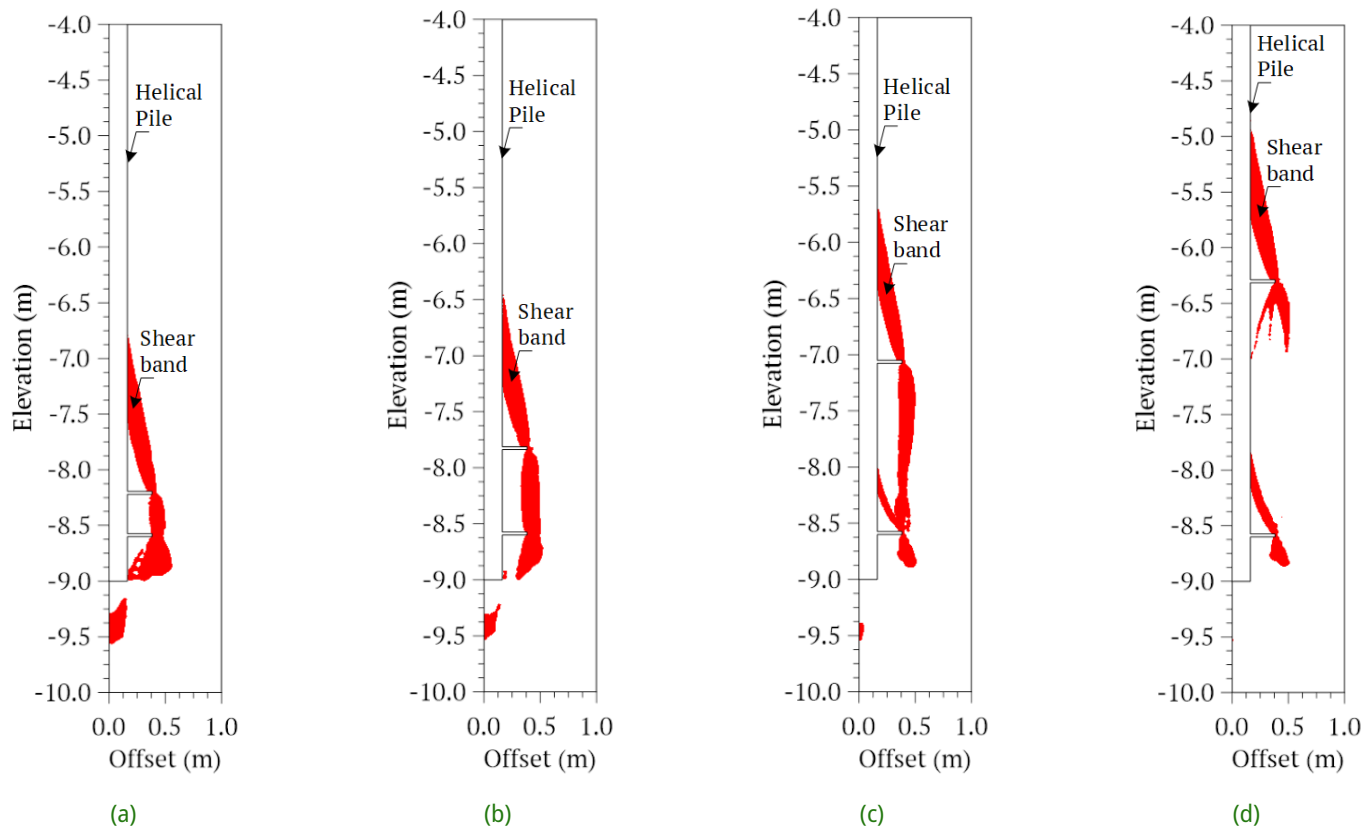
Figure 6 Shear bands around the helical piles embedded in dense sand with D = 762 mm and S_h/D = (a) 0.5, (b) 1, (c) 2, and (d) 3 at the pile head load equals 3341 kN
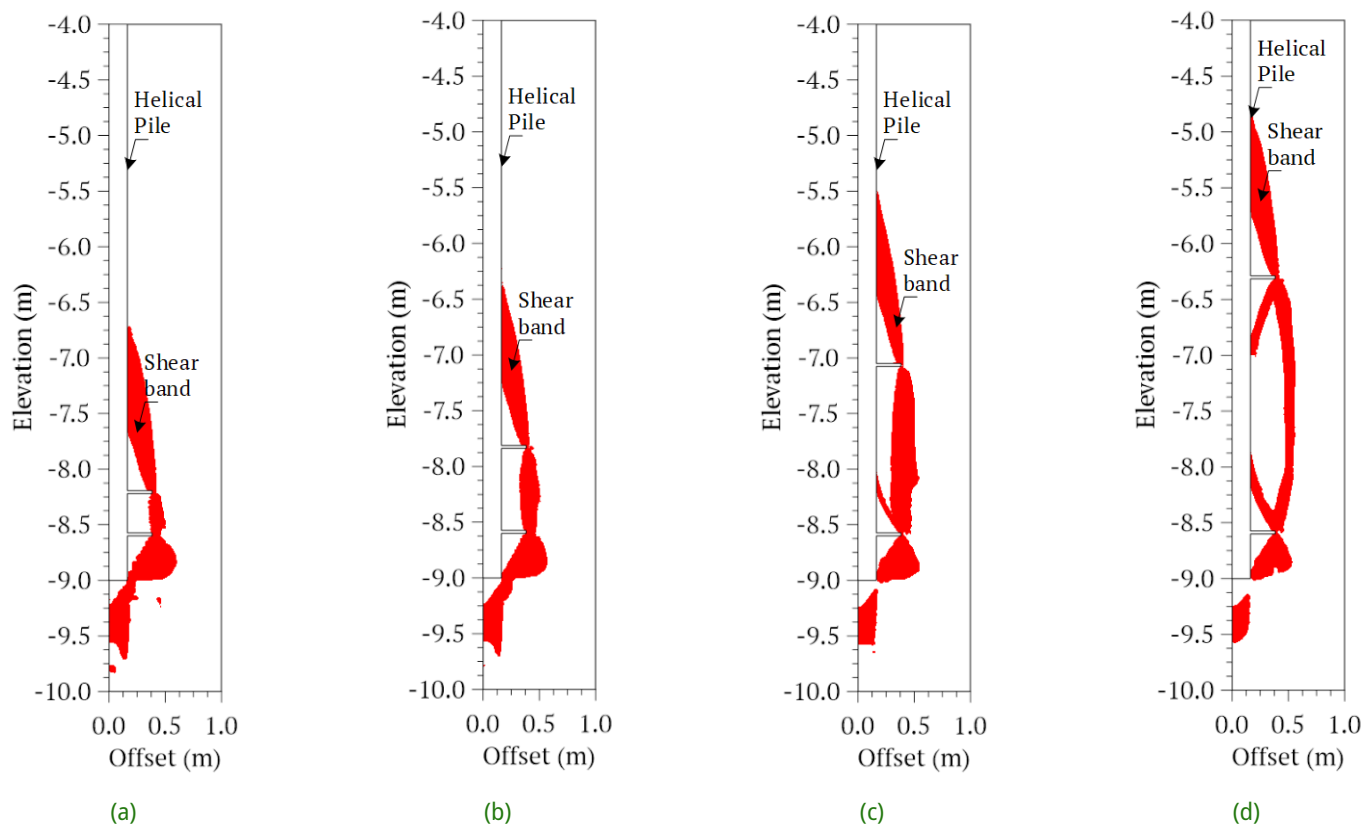

Figure 7 Shear bands around the helical piles embedded in stratified sand with D = 762 mm and S_h/D = (a) 0.5, (b) 1, (c) 2, and (d) 3 at the pile head load equals 2227 kN
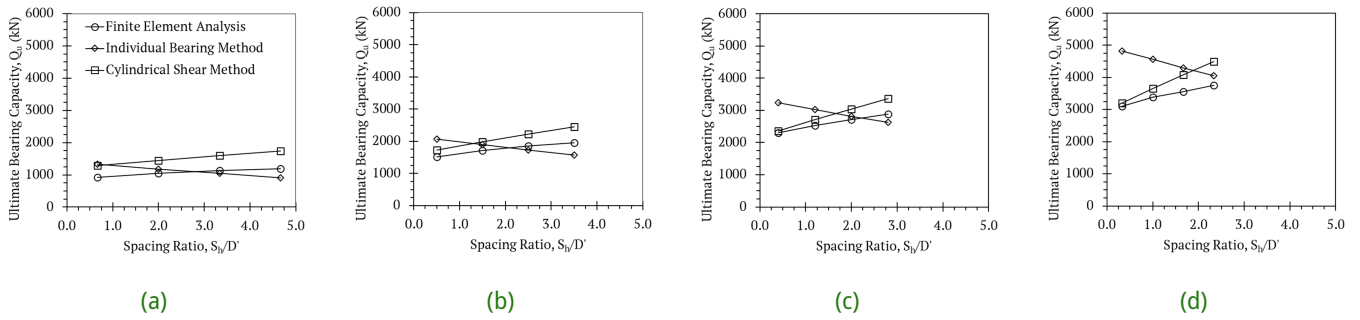
Figure 8 Changes of the ultimate bearing capacity (Q_u) for D'/D ratio (a) 0.75, (b) 1, (c) 1.25, and (d) 1.5

3.3 Effects of Helical Pile Diameter

Figure 8 illustrates the changes in the Q_u value corresponding to the variation of D'/D and S_h/D' ratios. Note that the S_h values in this section were kept consistent with those used in the previous analysis (see. Figure 4), but the helices diameter was varied. The results indicate that for each S_h/D' value, the Q_u values generally increased with the D'/D ratio. Conversely, for the same D'/D ratio, the $Q_{u,FE}$ and $Q_{u,CS}$ values increased with S_h/D' ratio, while the $Q_{u,IB}$ decreased as S_h/D' ratio increased. Additionally, the $Q_{u,FE}$ values were relatively close to the $Q_{u,CS}$ values, but it should be noted again that the shear failure model did not necessarily follow the CS failure model. These results were relatively similar to the previous findings presented in Figure 4. Referring to Equations (2) and (3), it is evident that if the diameter of the helical plates increased, then the Q_{cs} and Q_t values would also increase, leading to an increase in Q_u as well. Similar findings were also reported by Sprince and Pakrastinsh (2010).

The effects of helix diameter on the developing shear band were also examined by observing the γ_s contours around the helical piles. Figure 9 illustrates the shear band around the helical piles embedded in the stratified soil condition with $S_h/D' = 2$ and $D'/D = 0.75$, 1, 1.25, and 1.5. The results demonstrate that changing the helix's diameter influenced the transition of the helical pile failure mechanism. Specifically, the transition of the shear failure mechanism for a helical pile with a larger helix diameter occurred at a larger S_h/D ratio. As depicted in Figures 9a and 9b, for the cases with $D'/D = 0.75$ and 1, the transition of the shear band from the CS to IB failure model occurred at $S_h/D' = 2$. However, the developed shear band at $S_h/D' = 2$ for the $D'/D = 1.25$ and 1.5 cases, as shown in Figures 9c and 9d, formed a cylindrical shape following the CS failure model and remained apparent at $S_h/D' \geqslant 2$. The shear failure model started to become the IB failure model at $S_h/D' = 2.5$ for the $D'/D = 1.25$, whereas, for the $D'/D = 1.5$, the CS failure model was still evident at $S_h/D' = 2.3$. It is important to note that the numerical simulation for helical piles with $D'/D = 1.5$ in this study was only conducted up to $S_h/D' = 2.3$.

3.4 Helical Pile Load Transfer Mechanism

In this paper, the axial load transfer mechanism of the helical piles embedded in medium sand, dense sand, and the stratified soil conditions with various S_h/D ratios, as shown in Table 2, was also studied. The helical plate diameter (D) in this section was kept at 762 mm. The helical pile load transfer curves were then compared to those of the conventional piles where the pile had no helices, and the diameter of the pile was consistent with the helical pile shaft diameter, $d = 324$ mm.

Figures 10 to 12 display the axial compressive load transfer curves along the pile shaft for various applied loads at the pile head (Q) of the conventional piles and the helical piles with $S_h/D = 0.5$, 1, 2, and 3. The load transfer curves for helical piles with $S_h/D = 1.5$, 2.5, and 3.5 are not presented in this paper due to space limitations. In each figure, the same line color indicates the same load magnitude at the pile head, while the continuous line and the dashed line represent the load transfer curves for the helical pile and conventional pile, respectively. It is worth noting that there are no load transfer curves for the conventional pile with $Q = 1114$ kN in Figure 10 because the numerical simulation of the loading test on the conventional pile could not reach $Q = 1114$ kN.

The results depicted in Figures 10 to 12 revealed a relatively consistent trend. Analysis of the load transfer curves of the conventional piles in these figures indicates that the pile tip primarily carried the load at the pile head. On average, approximately 92% of the applied load (Q) was borne by the tip of the shaft (Q_{tip}), with the remainder supported by shaft resistance (Q_s). This relatively low shaft resistance may be attributed to a relatively low R_{inter} value and limited shaft surface area. Furthermore, Figures 10 to 12 demonstrate that the magnitude of the load transferred along the helical pile shaft above the upper helix was comparable to that observed for conventional piles. This finding suggests that the helices had a minimal or negligible effect on the magnitude of the load transferred to the helical pile shaft above the upper helix (first helix). The load carried by the shaft then significantly decreased at the helical plate locations, indicating that some of the
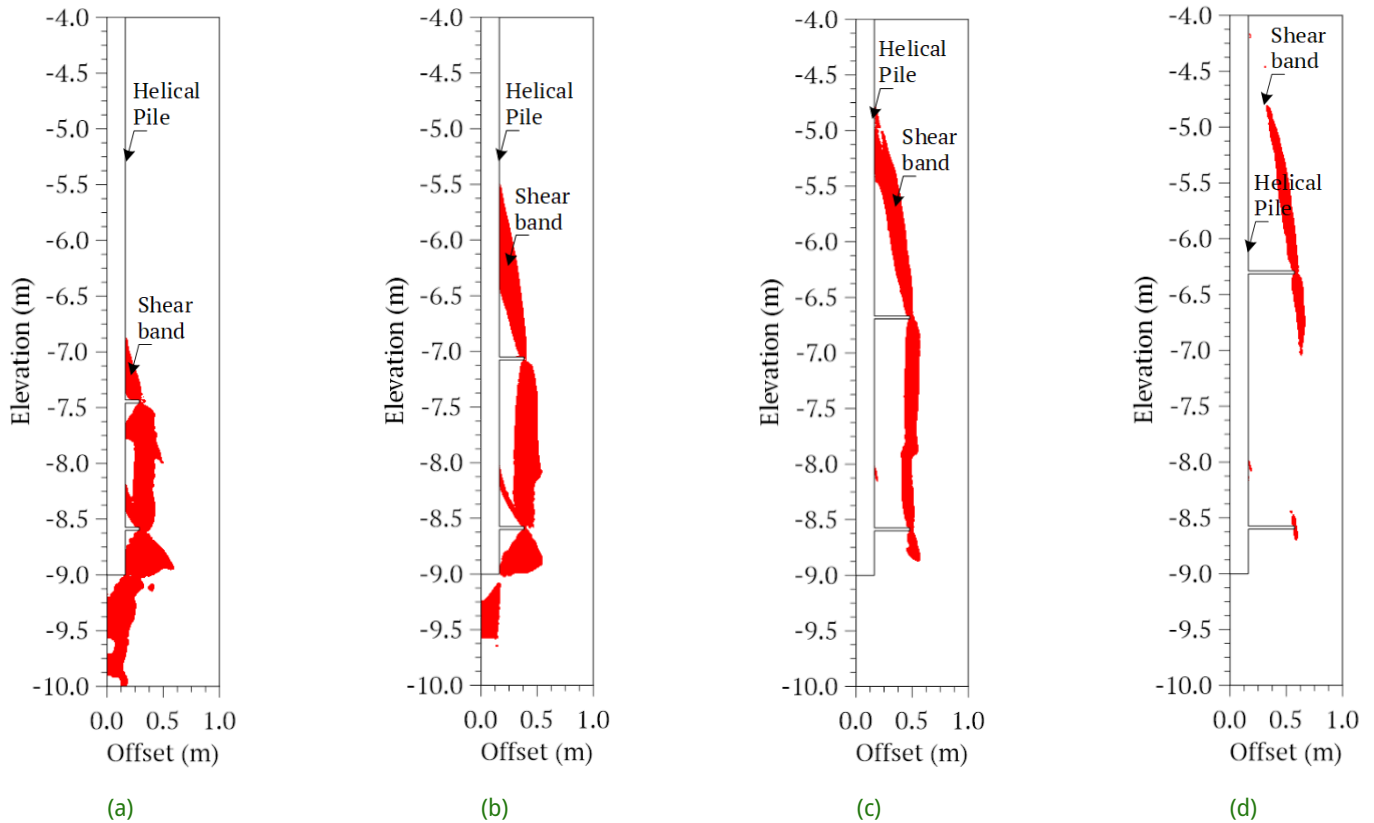
Figure 9 Shear bands around the helical piles embedded in stratified sand with S_h/D = 2 and (a) D'/D = 0.75, (b) D'/D = 1, (c) D'/D = 1.25, and (d) D'/D = 1.5 at the pile head load equals 2227 kN

load had been transferred to the helical plates (Figure 10b,c,d, Figure 11b,c,d, and Figure 12b,c,d). Notably, there was a smaller decrease in load observed at the upper helix compared to the lower helix (second helix), implying that the lower helix bore a larger load than the upper helix. This study estimated that, on average, the load carried by the upper helix ($Q_{h,2}$) was 31.3% of the applied load, while the load carried by the lower helix ($Q_{h,2}$) was 51.7% of the applied load. This finding suggests that approximately 83.1% of the applied load was borne by the helical plates. However, it is noteworthy that when S_h/D = 0.5 (Figure 10a, Figure 11a, and Figure 12a), the load carried by the pile shaft near the two helical plates steadily decreased, indicating that both of the helical plates behaved as one thick plate in carrying the load. It was estimated that the average load carried by the helical plates-soil combination was 73.4% of the applied load, while the shaft resistance supported the remainder. Ultimately, there was a significant decrease in the magnitude of the load transferred to the tip of the pile shaft, ranging from 8.3% to 17.4% of the load at the pile head. The typical measurements of Q_{tip}, $Q_{h,1}$, and $Q_{h,2}$ are illustrated in Figures 10 to 12.

The distribution of the load transferred along the pile shaft, as depicted in Figures 10 to 12, was insufficient for a clear classification of the helical pile failure mechanism (i.e., IB or CS models). The load transfer curves in Figures 10 to 12 demonstrate a relatively consistent trend, as explained earlier, except for the S_h/D = 0.5 cases, regardless of the occurred shear failure model. However, it is noteworthy that based on the presented load transfer curves, both the upper and lower helical plates continued to transfer the axial load from the pile head, even when the failure mechanism followed the CS model for the $S_h/D \leq 2$ cases. This finding suggests that the upper helix still contributed to the load-bearing capacity of a helical pile in the CS model. Furthermore, as the S_h/D ratio increased, it was also observed that the upper helix transferred a larger load, particularly evident in Figures 10d, 11d, and 12d, corresponding to the development of the IB shear failure model. This phenomenon was likely attributed to the closer proximity of the upper helix to the pile head, causing it to receive a larger load compared to other upper helices with a smaller S_h/D ratio.

Furthermore, Figures 10 to 12 demonstrate that a relatively small load was distributed along the pile shaft between the helical plates, which became larger for the S_h/D > 2 cases, where the IB failure model was indicated. This finding suggests that the pile shaft between the upper and lower helices transferred the load from the pile head to adjacent soil, and as a response, the soil provided frictional resistance. Thus, it was proposed to consider the shaft resistance in the Q_u calculations, especially in the $Q_{u,IB}$ formula. Considering the shaft resistance between the helices could increase the overall
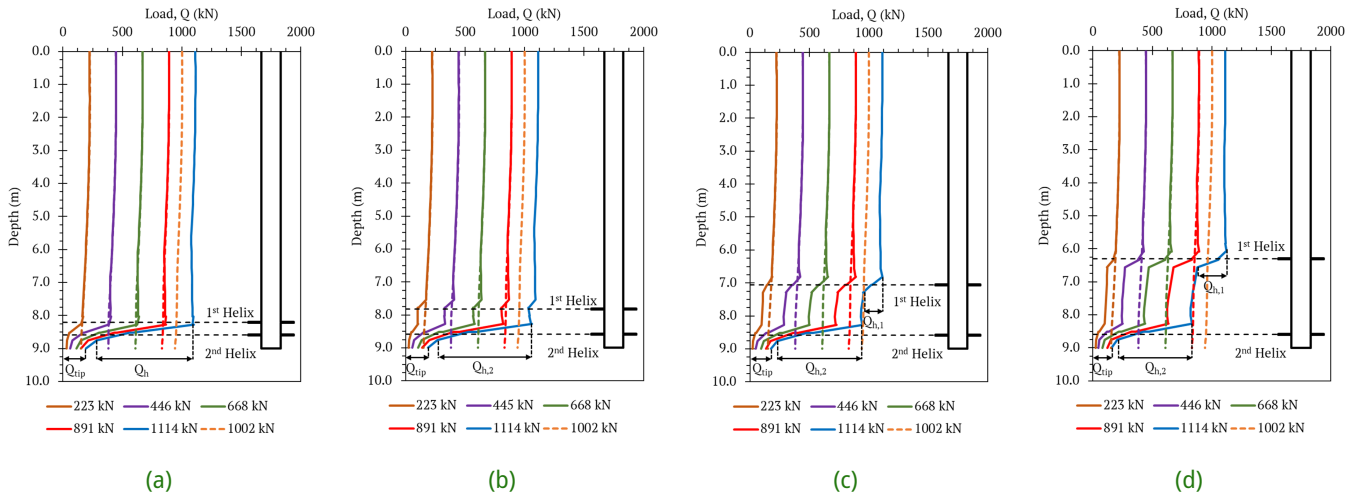
Figure 10 Load transfer curves on the shaft of the helical piles embedded in medium sand with D = 762 mm and S_h/D = (a) 0.5, (b) 1, (c) 2, and (d) 3
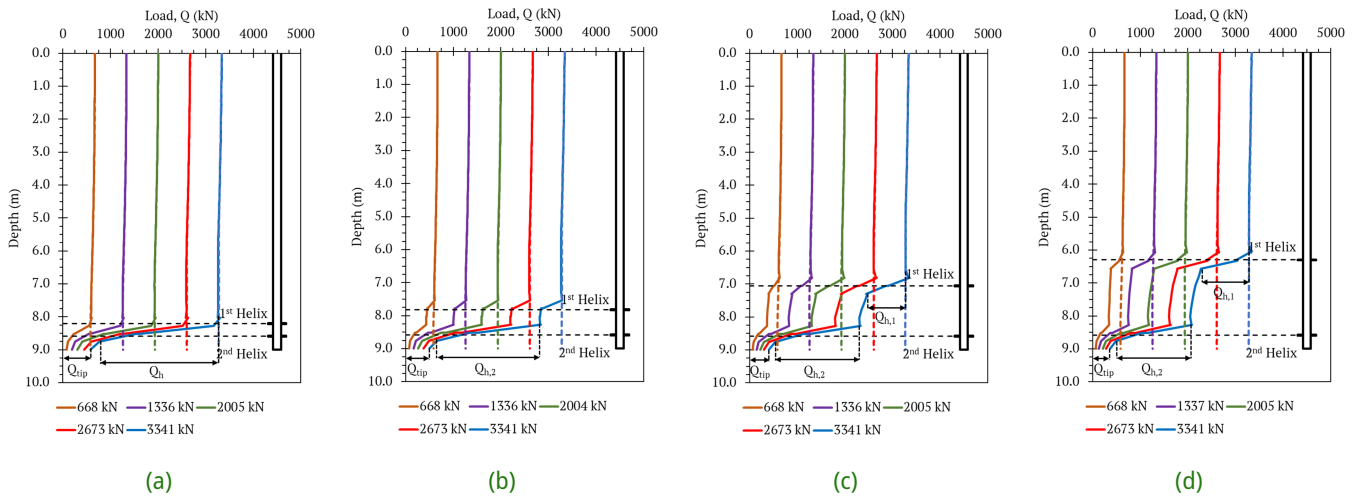

Figure 11 Load transfer curves on the shaft of the helical piles embedded in dense sand with D = 762 mm and S_h/D = (a) 0.5, (b) 1, (c) 2, and (d) 3

Q_u values, as illustrated in Figure 4 by the red dashed line.

4 CONCLUSION

This paper presented a series of numerical parametric studies on the effects of the spacing and diameter of helices on the ultimate bearing capacity and shear failure and load-transfer mechanisms of several helical piles embedded in cohesionless soils. The results showed that the helical pile's ultimate bearing capacity increased with the spacing and diameter of the helices. However, it was noted that the theoretical ultimate bearing capacities computed either by the individual bearing method or the modified equation tended to decrease with an increasing spacing of the helices due to the decrease of the bearing capacity of the upper helix as the spacing ratio increased.

Furthermore, the transition of the failure mechanism

of the helical piles from cylindrical shear to individual bearing models for the cases with the same helical plate diameter occurred at a spacing ratio of two. Then, increasing the diameter of helices shifted the spacing ratio where the failure transition occurred to a larger value, indicating a complex interplay between geometric parameters and failure mechanisms. It was thus suggested to directly observe the transition of the failure mechanism through either numerical simulation or laboratory model test.

The axial load transfer curves demonstrated a significant reduction in the load transferred to the pile tip with the addition of helical plates, as these plates partially carried the load. It was observed that the lower helix bore a larger load than the upper ones. Additionally, the load transfer curve was not clear enough to identify the failure mechanism of the pile. Despite indications of cylindrical shear failure, helical plates, particularly the upper helix, continued to transfer load
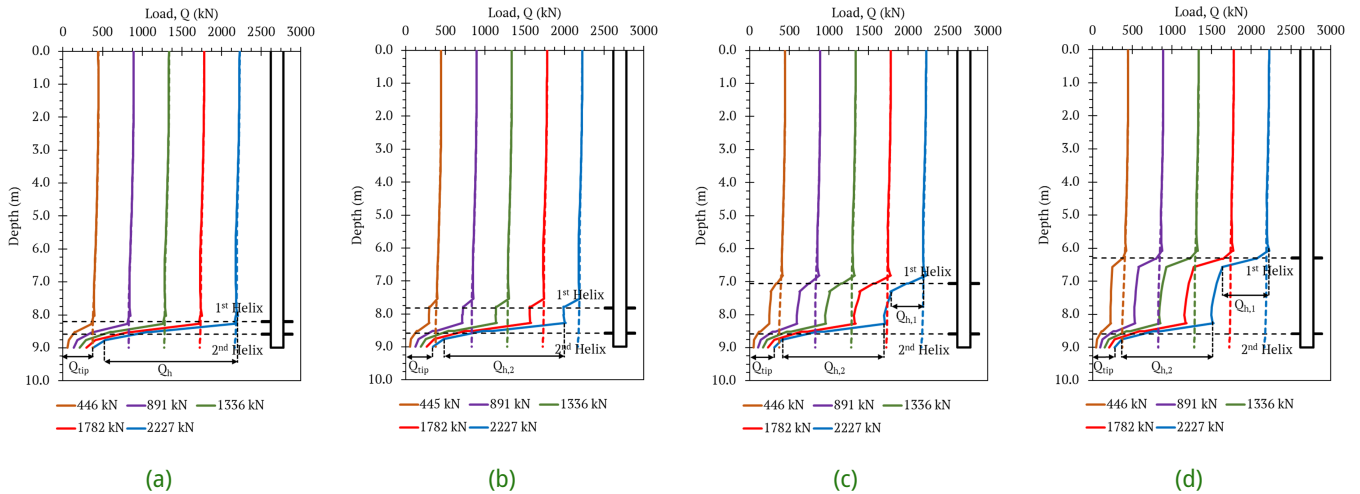
Figure 12 Load transfer curves on the shaft of the helical piles embedded in stratified sand with D = 762 mm and S_h/D = (a) 0.5, (b) 1, (c) 2, and (d) 3

to the soil . However, when the spacing ratio was sufficiently small, such as less than half of the helical plate diameter, the helical plates and soil between them behaved as a unified structure in carrying loads. As the spacing increased, leading to the development of the individual bearing failure model, the pile shaft between the helical plates transferred the load to the surrounding soil layer. Therefore, it was recommended to also consider the shaft friction between the helical plates in the calculation of the bearing capacity of a helical pile using the individual bearing method. Finally, the results of this study are applicable to helical piles with two helical plates embedded in relatively homogeneous cohesionless soil conditions. Further research, either through model tests or field tests, is necessary to validate the conclusions drawn in this paper.

DISCLAIMER

The authors declare no conflict of interest.

REFERENCES

Adams, J. I. and Klym, T. W. (1972), 'A study of anchorages for transmission tower foundations', *Canadian Geotechnical Journal* **9**(1), 89–104.
URL: *https://doi.org/10.1139/t72-007*

Alwalan, M. F. and El Naggar, M. H. (2021), 'Load-transfer mechanism of helical piles under compressive and impact loading', *International Journal of Geomechanics* **21**(6).
URL: *https://doi.org/10.1061/(ASCE)GM.1943-5622.0002037*

Bentley (2023), *PLAXIS 2D 2023.1: Material Model Manual 2D*.

Deardoff, D., Kortan, J., Malone, J., Olson, K. and Waltz, N. (2021), *Foundation Support Works Technical Manual*, 4th edn, Supportworks, Inc.

Elsherbiny, Z. H. and El Naggar, M. H. (2013), 'Axial compressive capacity of helical piles from field tests and numerical study', *Canadian Geotechnical Journal* **50**(12), 1191–1203.
URL: *https://doi.org/10.1139/cgj-2012-0487*

Fitriana, S. B. A. and Hamdhan, I. N. (2018), 'Pengaruh jumlah dan diameter helix terhadap daya dukung fondasi helical pile', *RekaRacana: Jurnal Teknil Sipil* **4**(1), 56.
URL: *https://doi.org/10.26760/rekaracana.v4i1.56*

Kulhawy, F. H. (1986), 'Limiting tip and side resistance: fact or fallacy?', *International Journal of Rock Mechanics and Mining Sciences & Geomechanics Abstracts* **23**(3), 108.
URL: *https://doi.org/10.1016/0148-9062(86)91224-6*

Livneh, B. and El Naggar, M. H. (2008), 'Axial testing and numerical modeling of square shaft helical piles under compressive and tensile loading', *Canadian Geotechnical Journal* **45**(8), 1142–1155.
URL: *https://doi.org/10.1139/T08-044*

Look, B. G. (2007), *Handbook of Geotechnical Investigation and Design Tables*, Taylor & Francis.

Lutenegger, A. (2009), 'Cylindrical shear or plate bearing uplift behavior of multi-helix screw anchors in clay', pp. 456–463.
URL: *https://doi.org/10.1061/41021(335)57*

Lutenegger, A. J. (2011), Behavior of multi-helix screw anchors in sand, *in* '2011 Pan-Am CGS Geotechnical Conference: 64th Canadian Geotechnical Conference and 14th Pan-American Conference on Soil Mechanics and Geotechnical Engineering'.

Mitsch, M. P. and Clemence, S. P. (1985), Uplift capacity of helix anchors in sand, *in* S. P. Clemence, ed., 'Unknown Host Publication Title', American Society of Civil Engineers (ASCE), pp. 26–47.

Mohajerani, A., Bosnjak, D. and Bromwich, D. (2016), 'Analysis and design methods of screw piles: A review', *Soils and Foundations* **56**(1), 115–128.
URL: *https://doi.org/10.1016/j.sandf.2016.01.009*

Mooney, J. S., Adamczak Jr., S. and Clemence, S. P. (1985), Uplift capacity of helical anchors in clay and silt, *in* S. P. Clemence, ed., 'Uplift Behavior of Anchor Foundations in Soil', American Society of Civil Engineers (ASCE), pp. 48–72.

Nabizadeh, F. and Choobbasti, A. J. (2017), 'Field study of capacity helical piles in sand and silty clay', *Transportation Infrastructure Geotechnology* **4**(1), 3–17.
URL: *https://doi.org/10.1007/s40515-016-0036-0*

Nasr, M. H. (2004), Large capacity screw piles, *in* 'The International Conference: Future Vision and Challenges for Urban Development', pp. 1–15.

Perko, H. A. (2009), *Helical piles: a practical guide to design and installation*, John Wiley & Sons, Inc.

Rao, S. N., Prasad, Y. V. S. N. and Shetty, M. D. (1991), 'The behaviour of model screw piles in cohesive soils', *Soils and Foundations* **31**(2), 35–50.
URL: *https://doi.org/10.3208/SANDF1972.31.2_35*

Reese, L. C. and O'Neil, M. W. (1988), Report no. fhwa-hi-88-042 - drilled shafts: Construction procedures and design methods, Technical report.

Sakr, M. (2009), 'Performance of helical piles in oil sand', *Canadian Geotechnical Journal* **46**(9), 1046–1061.
URL: *https://doi.org/10.1139/T09-044*

Sakr, M. (2011), 'Installation and performance characteristics of high capacity helical piles in cohesionless soils', *DFI Journal - The Journal of the Deep Foundations Institute* **5**(1), 39–57.
URL: *https://doi.org/10.1179/dfi.2011.004*

Salhi, L., Nait-Rabah, O., Deyrat, C. and Roos, C. (2013), 'Numerical modeling of single helical pile behavior under compressive loading in sand', *Electronic Journal of Geotechnical Engineering* **18**, 4319–4338.

Soltani-Jigheh, H. and Zahedi, P. (2020), 'Load transfer mechanism of screw piles in sandy soils', *Indian Geotechnical Journal* **50**(6), 871–879.
URL: *https://doi.org/10.1007/s40098-020-00431-5*

Sprince, A. and Pakrastinsh, L. (2010), Helical pile behavior and load transfer mechanism in different soils, *in* '10th International Conference "Modern Building Materials, Structures and Techniques,"', pp. 1174–1180.

Trofimenkov, J. G. and Mariupolskii, L. G. (1965), Screw piles used for mast and tower foundations, *in* 'The 6th International Conference on Soil Mechanics and Foundation Engineering', pp. 328–332.

Vignesh, V. and Mayakrishnan, M. (2020), 'Design parameters and behavior of helical piles in cohesive soils—a review', *Arabian Journal of Geosciences* **13**(22), 1194.
URL: *https://doi.org/10.1007/s12517-020-06165-1*

[This page is intentionally left blank]